High-efficiency cryo-thermocells assembled with anisotropic holey graphene aerogel electrodes and a eutectic redox electrolyte

Guangyong Li[†], *Dapeng Dong*[†], *Guo Hong*[†], *Lifeng Yan, Xuetong Zhang*, Wenhui Song**

G. Li, D. Dong, Prof. X. Zhang
Suzhou Institute of Nano-Tech and Nano-Bionics, Chinese Academy of Sciences, Suzhou, 215123, P.R. China.
E-mail: xtzhang2013@sinano.ac.cn
G. Li
School of Materials Science and Engineering, Beijing Institute of Technology, Beijing, 100081, P. R. China.
Prof. G. Hong
Institute of Applied Physics and Materials Engineering, University of Macau, Macao.
Prof. L. Yan
Department of Chemical Physics, University of Science and Technology of China, Hefei 230026, P.R. China
Prof. X. Zhang, Prof. W. Song
Centre for Biomaterials in Surgical Reconstruction and Regeneration, Division of Surgery and Interventional Science, University College London NW3 2PF, United Kingdom.
E-mail: w.song@ucl.ac.uk

† These authors contributed equally to this work.

Abstract: Thermocells, capable of converting temperature-dependent electrochemical redox potentials into electrical power, can harvest waste or low-grade heat in an economical and continuous approach with zero carbon emission. However, the power density and conversion efficiency of thermocells are hindered by a narrow operation window and low ion conductivity of the electrodes, especially in freezing weather conditions. Herein, highly efficient cylindrical thermocells, working in a wide operation window of cold temperatures, have been developed. A eutectic electrolyte consisting of formamide and water has been formulated with a high ion conductivity, which is retained at a significantly extended lower limit of the operation window

1

from conventional 0 °C to −40 °C for the first time. In parallel, an electrode material based on anisotropic holey graphene aerogel has been synthesized with improved ion conductivity, especially at temperatures below 0 °C, due to its aligned graphene sheets and pores. By taking the advantages of both components, the power density and the Seebeck coefficient of a single cylinder thermocell reaches an exceptionally high value, i.c. 3.6 W/m^2 and 1.3 mV K^{-1}, respectively. Moreover, assembled thermocells in series packaging substantially enhance the voltage of the open-circuit, i.e. from 140 mV (1-cylinder thermocell) to 2.1 V (15-cylinder thermocells).

Sustainable renewable energy resources are promising to mitigate the exhaustion of fossil fuels and the urgency of the global energy crisis, and to meet energy demand for future generations. [1] Low-grade heat, [2] including the waste heat from industrial streams, solar panels, geothermal reservoirs, the human body, and electronic devices dissipation, is an attractive energy source given by its abundance and accessibility. Generally, most of this low-grade heat is wasted which leads to a series of environmental problems.[3] As more low-power driven portable/wearable smart electronic device emerge in the fast growing global civil and military markets, the sustainable energy scavenged from body heat and surrounding environment become appealing to either replace or augment battery usage. Thermoelectric systems [4] are capable of converting thermal energy into electrical energy. Conventional thermoelectric generators, [5] utilising the Seebeck effect (Se), are mainly based on semiconductors, suffering pristinely low efficiency, rare and brittle materials and complicated fabrication processes. Alternatively, aqueous electrolyte systems (**Figure**

1a), [6] based on redox reactions, have recently received great attention due to their high power-density and easy scaling-up.

Recent revival on the development of electrochemical thermocells has been driven by the rapid progresses on the relevant electrolyte materials, nanostructured electrodes and interface optimization, which has been recently reviewed [6c] and summarised in Supporting Information (Table S1). In theory, the power density of a thermocell is determined by the temperature difference (ΔT) between the heat source and the heat sink and ion conductivity of the electrode, which dominates the short circuit current [4, 6c]. Generally, the operation window of a thermocell with an aqueous electrolyte working from the freezing point (0 ^{o}C) to the boiling point (100 ^{o}C) of water, means that the maximum temperature difference between the heat source and sink is 100 ^{o}C. To extend the upper limit of the temperature window, various solvents with a higher boiling point, i.e. ionic liquids, [7] are introduced into thermocell systems. Nevertheless, ionic liquids are highly viscous at room temperature that slows down ions diffusion and thus results in high electrical resistance. Alternatively, the operation window can be widened by extending the lower limit. Inspired by the nature of a eutectic mixture,[8] that has a lower freezing point than any of its components, electrolytes consisting of a eutectic mixture solvent was reported to improve the capacitive charge storage at a sub-zero temperature. [8c] In addition to the extended temperature window for achieving the high power density, the low temperature thermocells are of strategic importance in severe winter and harsh polar environments. However, overcoming the reduction of conductivity and low transmission rates of ions of the electrolyte at low temperatures is the major challenge.

3

The desired electrode materials, which can provide the mass transport channel and charge transport network, are indispensable for the high-power density and conversion efficiency of electrochemical energy system. [9] Graphene aerogel, [10] with an intrinsically high specific surface area，continuous thermal and electrical conductivity networks, has demonstrated unparalleled advantages as an electrode material in an electrochemical energy system. However, due to the instinctive random-stacking of graphene sheets during the sol-gel process of graphene oxide (GO) solution, the traditional graphene aerogel usually consists of disordered graphene porous network, which undermines the ions/charge transmission in electrode. [11] Recently, a GO liquid crystal (GO-LC) with long-range ordered graphene sheets has been developed. [12] However, similar to both liquid crystalline molecules, polymers and particles, [13] GO-LC are bound to self-assemble locally into multi-domain microstructures with inherent disclinations, resulting in wrinkles and cracks in GO-LC derived 3D graphene monolith materials. [14] On the other hand, it is well known that molecular chains and particles in the liquid crystalline phase are inclined to align uniformly under a boundary effect or external mechanical/electrical field. [15] Highly oriented graphene based functional materials, such as graphene fibre and graphene film, have been fabricated from GO-LC. [12] GO-LC can also serve as an optimal gelation precursor for graphene aerogel. Therefore, to produce the gelation of uniform and globally oriented GO-LC for ideal graphene based electrode materials with regular pore channel/wall (of benefit to ion/charge transportation) is highly desired and potentially achievable.

Herein, an efficient cryo-thermocell system (Figure 1a) has been developed by assembling a new electrode material (Figure 1b) and electrolyte (Figure 1c) together to tackle the above challenges. Specifically, a mixture of formamide and water (FA-H_2O, 1:1, v:v) with a freezing point of −44 °C [8c] was formulated as an electrolyte with the addition of $K_3Fe(CN)_6$/$(NH_4)_4Fe(CN)_6$ as redox mediator, which raised the saturated concentration, and thus enhanced ion concentration at low temperatures. Meanwhile the anisotropic holey graphene aerogel (AHGA) electrodes were designed and fabricated. The interpenetrating micropores and mesopores throughout the ordered array of AHGA network improved the ion transfer channels through reduction of the ion transport path and transmission impedance. As a testing vehicle, a columnar thermocell was assembled and tested with the heat sink maintained at −40 °C, which demonstrated the outstanding power density and the Se value, 3.6 W/m^2 and 1.3 mV K^{-1}, respectively. To the best of our knowledge, it is the first time to report that a single column thermocell works with high efficiency at such low temperatures. Furthermore, the voltage output up to 2.1 V of the assembled 15-thermocells in series packaging proved the feasibility of scale-up, promising important application prospects in large-scale wearable devices in freezing weather.

Figure 1a shows the working mechanism of the cryo-thermocell. Two identical AHGA electrodes are in contact with an eutectic electrolyte containing a redox couple and lead to an external circuit. When the temperature varies across the cell, the electrical power will be generated due to a difference of the redox potential of the electrolyte between the two electrodes driven by the temperature gradient. (more details see Method in the Supporting Information)[6].

Schematic synthesis of the AHGAs was depicted in Figure 1b. Holey graphene oxide (HGO) was first synthesized via a facile mild defect-etching reaction.[16] HGO solution was obtained briefly by heating a homogeneous aqueous mixture of graphene oxide (GO) and H_2O_2 at 100 °C under stirring. A mass of in-plane pores with sizes of a few nanometres across the whole HGO nanosheet was observed in the images by transmission electron microscopy (TEM)(**Figure 2b**). The pore size could be adjusted by controlling the etching time (Figure S1). No pores were observed on the GO sheets (Figure 2a) after the same treatment without H_2O_2, which suggests that carbon atoms in GO sheets became more vulnerable to be etched by H_2O_2.[16b] Unexpectedly, HGO has a slightly lower intensity ratio of D/G peaks (I_D/I_G=0.87) compared to that of GO (I_D/I_G=0.91) in the Raman spectra as shown in Figure 2e, which may indicate that HGO possesses fewer oxygen function group and defects despite the generation of nano-pores. After high-speed centrifugation, HGO suspensions exhibited a bright birefringence texture under a cross-polarized light microscope, reflecting the formation of the lyotropic liquid crystalline phase (Figure 2d and Figure S2-S3), similar to the anisotropic GO aqueous suspension (Figure 2c). More uniform long-range ordered assembling of the holy graphene hydrogel was induced by the shear force applied through the syringe piston.[12a] The uniform alignment in the anisotropic holey graphene hydrogels was further enhanced due to the capillary effect within the syringe piston via *in situ* reduction of oriented holey graphene oxide with vitamin C in the annealing process in a 30 °C water bath for 72 hours (Figure S3). The resulting hydrogels were washed three times with ethanol, subsequently dried with supercritical CO_2 fluid, and finally heated at 900 °C in argon for 6 hours to form cylinders of AHGA, as shown in Figure 2f.

The resulting AHGA cylindrical rod with the volume of ca. 0.5 cm^3 could stand on a soft lily flower petals without being bended (Figure 2f), indicating the ultra-light-weight nature of the AHGA. The apparent density of the aerogel was tested in the range of 42~55 mg·cm^{-3}, which varied with the etching time (Figure S4) similar to graphene aerogel (GA, with the density of ~46 mg cm^{-3}), anisotropic graphene aerogel (AGA, ~48 mg cm^{-3}), and holey graphene aerogel (HGA, ~66 mg cm^{-3}) reported elsewhere.[11,14a,16-17]. The anisotropic porous morphology was further confirmed by scanning electron microscopy (SEM). Figure 2g and Figure S5 in supporting information reveal that the edges of the holy graphene sheets were packed in a circumferential orientation on the fracture surface perpendicular to the long axis of the AHGA cylinder, which was induced by the shear force of the syringe piston and the tubular boundary effect of the syringe during annealing. The close-up view of Figure 2g inset and Figure S5 show that the honeycomb-like pores align between the parallel graphene sheets in a form of a three-dimensional layered network. This is in consistence with the parallelly stacked holy graphene sheets which form flat pore walls (Figure 2h and Figure S5 in supporting information) observed from the fracture surface, parallel to the long axis of the cylinder. In addition, the aligned structure appeared to become random as increasing the etching time (Figure S6-S7), mainly because more defects and size reduction in the graphene sheets were generated during the long etching process. As a result, great distortion of the graphene sheets occurred during subsequent carbonization (Figure S8).

The AHGA samples exhibited direction-dependent mechanical properties, as shown in Figure 2i-2j. The compression yield strength in the axial direction reached ~0.7 MPa, two times higher than that in the radial direction (~0.29 MPa, more details in the Supporting Information), similiar

to that of the AGA (aligned aerogel with non-etching graphene sheets, ~0.75 MPa),[14a] and much higher than that of conventional GA reported elsewhere (0.04-0.16 MPa).[11,12c,18] For instance, the resulting aerogel could support a counterpoise, which is more than 13000 times its own weight, as shown in the inset of Figure 2i. The electrical conductivity of the resulting aerogel also exhibited to be anisotropic in nature (Figure 2j). The electrical conductivity along the axial direction is 165 S/m, which is about five times higher than that of the radial direction (35 S/m), and three times higher than that of conventional GA.[11,12c,14b,18c,18d]

The porous structures of AHGAs were investigated by using nitrogen sorption spectra (Figure S9 and Table S2). HGO aerogels exhibited a high specific surface area, nearly twice that of the GO aerogels (Figure 2k). The specific area of AHGA increased along with the etching time and could reach up to 825 m^2g^{-1}. Such a high specific surface area of AHGA was mainly attributed to the introduction of nanopores and wrinkles in the graphene sheets which could undermine the plane-plane stacking between the graphene sheets during assembling (Figure S10). Furthermore, the anisotropic porous structure with aligned pores and holy walls of AHGA could reduce the resistance of ion transportation, which is a desirable electrode material for energy storage and conversion.

Apart from the aforesaid advanced nano-carbon material electrode, a suitable electrolyte is also an important component of the thermocell.[7,19] An ideal electrolyte is one that can adapt to the various climates and effectively improve the performance of the thermocell spanning over a wide range of working conditions. A new eutectic mixture (Table S1), containing formamide and water (FA-H_2O) as the solvent and potassium ferricyanide and potassium ferrocyanide ($K_3Fe(CN)_6$/$(NH_4)_4Fe(CN)_6$) as solutes (Figure 1c), was formulated as an electrolyte, which was

capable of maintaining non-coagulation at −40 ºC with the conductivity reaching as high as 5.1 mS/cm. The electrical conductivity of the electrolyte was tested as a function of the concentration under −40 ºC, as shown in **Figure 3a**, which increased along with the concentration initially, peaked at a concentration of 0.4 M. The conductivity appeaed to level off with some viaraiton as further increased above to the satuated concentration. A slight decrease of the conductivity was tested at a concentration of 0.5 M, which may be contributed to the crystallization of the solutes (Figure 3a). It is of note that such crystallization should be avoided due to potentially unexpected safety problems such as short circuiting.

The conductivity of the optimized 0.4 M electrolyte was tested under a wide range of temperature from −40 ºC to 100 ºC (Figure 3b). As expected, the ionic conductivity increased as the temperature of the electrolyte solution was elevated, with exceptionally high values retained when the temperature was below zero. For instance, the conductivity is 5.1 mS/cm at −40 ºC, which is 5 times higher than that of the gel electrolyte[20] (1.01 mS/cm) and 17 times higher than that of ionic liquids electrolyte[21] (0.3 mS/cm) at room temperature. Moreover, this organoaqueous electrolyte has better wettability and infiltration to the electrode material contributed by their strong ionic interaction, compared to the conventional aqueous electrolyte (Figure S11), which facilitates the transition of ions between the electrolyte and electrodes.

The Seebeck coefficient (Se) of the electrolyte was obtained in a U-shaped cell, as in our previous report,[6a] which was 1.3 mV/K under the proposed circumstance (Table S1). This is the highest among any existing electrolytes, such as $[FeCl_4]^-/[FeCl_4]^{2-}$ (0.48 mV/K), $[Fe(bpy)_3]^{3+}/[Fe(bpy)^3]^{2+}$ (0.48 mV/K), $[Cr(bpy)_3]^{3+}/[Cr(bpy)_3]^{2+}$ (0.43 mV/K) redox couples reported elsewhere[22] and the most studied thermoelectric materials such as bismuth telluride[19]

9

(0.287 mV/K) and antimony telluride[23] (0.135 mV/K) (Table S1). This result was further confirmed by changing the rate of formal potential as a function of temperature. The thermoelectric voltage from the thermocell was generated by the temperature dependence of the redox potential[19]. Hence, the change rate of the formal potential of the redox couples as a function of temperature is correlated to the Se coefficient. Figure 3d shows the changes in the formal potential of the redox couples as a function of temperature. From the gradient of the fitted lines, the Se of the redox couples was determined again to be 1.3 mV/K, which is consistent with the result from the U-shaped cell measurements.

The anisotropic structure and properties of the AHGA characterized above have demonstrated great potential as an electrode material with high electrochemical performance (Table S1). Generally, there is a trade-off between the high specific surface area and ion transport for porous material-based electrodes, in that the desired high specific surface area of the pore structure may impede deeper ion transport into the electrode due to its high tortuosity of the isotropic and random pores, as shown in Figure 1a and **Figure 4a**. In contrast, the well-aligned holey graphene sheets in the aerogel are hypothesized to offer more electrochemically active sites as well as faster ion transport within the aligned porous channels, as schematically illustrated in Figure 4b. Cyclic voltammetry (CV) and electrochemical impedance spectroscopy (EIS) were used to validate the hypothesis of the potentially outstanding electrochemical properties of AHGA. The real electro-active surface area (ESA) of the aerogel working electrode can be derived from the Randles - Sevcik equation[24] given by:

$$I_p = 2.69 \times 10^5 \times ESA \times D^{1/2} \times n^{3/2} \times v^{1/2} \times C \tag{1}$$

where I_p is the faradaic peak current, D the diffusion coefficient, n the number of electrons transferred during the redox reaction, v the potential scan rate, and C the concentration of probe molecule. In Figure 4c, the faradaic peak current of the AHGA is the highest among the other three types of aerogels including HGA, AGA, and GA. The AHGA electrode was reported to possess a high ESA, which may be ascribed to the introduction of nanopores on the graphene sheets.[6a] On the other hand, well-aligned holey graphene sheets in the aerogel electrode could effectively improve ion transport efficiency,[25] which is confirmed by the Nyquist plot in Figure 4d. The Nyquist plots of the aerogel electrodes exhibits a response that is controlled by a combination of reaction kinetics and diffusion.[26] The charge transfer resistance (RCT) could be estimated from the diameter of the semicircle in the Nyquist plot according to the Randles model.[26] The segment of the Nyquist plot approaching 45° in the high-medium frequency range is indicative of the ion diffusion impedance.[26] The RCT value of the AHGA, HGA, AGA, and GA is 5.1 Ω, 8 Ω, 4.5 Ω, and 5.7 Ω, respectively, indicating that well-aligned graphene sheet structure is beneficial to the charge transport. The ion diffusion impedance of the AHGA electrode (15.7 Ω) is much lower than that of the HGA electrode (29 Ω), AGA electrode (34 Ω) and GA electrode (47 Ω), indicating more rapid ion diffusion occurs within AHGA due to its aligned pore structure and hierarchical porosity.[14] The superior electrochemical properties of AHGA in terms of the remarkably high ESA and low ion transmission impedance promise an ideal electrode material for a thermocell.

The AHGA aerogel and the $Fe(CN)_6^{4-}/Fe(CN)_6^{3-}$ electrolyte were packaged in a polytetrafluoroethylene tube and assembled into a single columnar thermocell. For all the thermocell testing in this work, the heat sink was always kept at −40 °C and the heat source was

verified by controlling the heating belt. The highest temperature difference tested for the AHGA

columnar thermocell reached 106 °C as shown in Figure 4e-f and Table S1, which is the highest

among those reported in literature (more details in Table S1). The corresponding open-circuit

voltage was 140 mV, which is two times higher than that of a conventional aqueous electrolyte

based thermocell (72 mV).[24] The power density of the single thermocell reached 3.6 W/m^2

(Figure 4f), which is nearly three times that of the activated carbon cloth electrode (1.2 W/m^2).[27]

The electrode-mass-normalised power reached 6.8 W/Kg, which increased by 76% compared to

that of the reduced graphene oxide electrode based (3.87 W/Kg) and by 30% compared to the

single wall carbon nanotube electrode based (5.2 W/Kg) [6b]. The energy conversion efficiency of

the single thermocell column relative to the Carnot engine reached to 0.7%, which is almost

twice as high as that of other electrochemical thermocells[27] (0.4%). The temperature difference

between the electrodes, the Seebeck coefficient and thermal conductivity of the electrolyte, and

the microstructure and conductivity of the electrode materials could affect the efficiency of the

thermocell. In comparison, the fabrication and characterisation of the single columnar thermocell

based on other electrode materials, including HGA, AGA and GA, was also carried out, as

shown in Figure S12. The highest output in terms of the potential and power density of each

thermocell, based on different electrodes under the same conditions with the largest temperature

difference being 106 °C, are demonstrated in Figure 4g and 4h. Figure 4h shows that the power

density of the AHGA electrode (3600 mW/m^2) is twice that of the HGA electrode (1586

mW/m^2), three times that of the AGA electrode (1015 mW/m^2), and six times that of the GA

electrode (564 mW/m^2). The outstanding performance of the AHGA based thermocell further

proves that the unique structure and properties of the AHGA electrode, in combination with the

superior ionic conductivity of the electrolyte have substantially enhanced the electrochemical performance in a wide operation window.

Although the performance of a single thermal electrochemical cell column has been greatly improved compared to previous reports (Table S1)[6a], its narrow output potential is still beyond the requirement for practical uses. The assembly of more AHGA cylinders was studied as shown in Figure S13. Two cylindrical thermocells were connected in series and in parallel, respectively. As expected, the output voltage of two-cylinder themocells in series was doubled, while the output current density of the two-cylinder thermocells in parallel was doubled also. Based on this excellent integrability, fifteen-cylinder thermocells were assembled in series into a facile low temperature thermocell device as shown in **Figure 5a**. The output power and potential of the assembled thermocell device were effectively improved (Figure 5b). The output voltage of the assembled thermocell device was increased fifteen times, from 140m V (1 thermocell) to 2100 mV (15 thermocells), while the maximum output power was improved by five times from 0.07mW (1 thermocell) to 0.37 mW (15 thermocells). The energy conversion efficiency of the thermocell device relative to the Carnot engine reached to 0.26%, which is comparable to U -thermocell based on carbon nanotube electrode (0.275%)[6b]. The relative energy conversion efficiency of the thermocell device is lower than that of single thermocell column, which ascribes to that the internal resistance was involved in the assembling process of multiple thermocells.

In addition, when the temperature of the heat source was close to the temperature of the human body (36-37 °C), the temperature difference between the electrodes can reach 35 °C. The low temperature thermocell device output voltage was 690 mV and the output power was 24 μW,

13

respectively (Figure 5c), which is comparable to other types of energy harvesting devices (30.97 μW) based on carbon nanotube fibres[28]. Therefore, such a low temperature thermocell device has great prospects in applications of wearable devices, especially in extremely cold environments. The output potential of the assembled cryo-thermocell device reached 2.1 V when the temperature difference between the electrodes was elevated to 106 °C. Furthermore, the output of the cryo-thermocell remained fairly constant for 600 seconds (Figure 5d). The high output potential of the device was much higher than that of the moisture-enabled electricity generator[29] (1.3V). Compared to the thermoelectric devices reported, the output voltage of this device (2.1V) was higher than that of the carbon nanocomposite textile-based devices reported elsewhere (1.3V) [30], and the output power was eighty times higher than that of the gel-electrolyte-based device (0.3 μW)[31]. As a testing vehicle, the device could directly light up two LED beads without using a converter circuit for a conventional battery system, as shown in the inset of Figure 5d and Figure S14 in Supporting Information. Finally it is of note that the cylinder thermocell renders a controllable cell orientation and adjustable electrode spacing simultaneously. Its cylindrical shape also benefits to the integration and optimisation of a series packaging of the cells for practical application.

In summary, the holey graphene sheets have been successfully assembled into a bulk anisotropic aerogel via *in situ* reduction of a holey graphene oxide liquid crystal. The high specific surface area (537~836 m^2/g) and low density (42~55 mg/cm^3) of the anisotropic aerogel, plus its aligned graphene sheets and porous structure in the form of cylinder electrode contribute to its outstanding electrochemical properties, compared to other carbon nanostructured electrodes reported in the literature. A eutectic mixture of formamide and water as a solvent has also been

developed and optimized to maintain fluidity and remarkably high ionic conductivity (5.1 mS/cm) at a low temperature of -40 °C. The first high performance thermocell made from the anisotropic holey graphene aerogel electrode based single thermocell and the new electrolyte is capable of working at low temperature, *i.c.* -40 °C. The single thermocell possesses high power density of 3.6 W/m^2 and Se of 1.3 mV K^{-1}. Moreover, a series of single thermocells have been assembled into a device package. In the case of a serial thermal cell made up of 15 AHGA cylinders , the voltage output in the open-circuit has been substantially increased from 140 mV of a single-cylinder thermocell to 2.1 V, which provides a bright prospect in wearable devices and field energy supplies in extremely cold environments.

Experimental Section

Materials: Graphite (crystalline powder, 400 mesh), phosphorus pentoxide (P_2O_5), potassium permanganate ($KMnO_4$), hydrogen peroxide (H_2O_2), sulfuric acid (H_2SO_4), and ascorbic acid (VC) were purchased from Sinopharm Chemical Reagent Company. Potassium ferricyanide ($K_3[Fe(CN)_6]$) and ammonium ferrocyanide (($NH_4)_4[Fe(CN)_6]$) were supplied by J&K Scientific Chemical Reagent Company. All chemicals were used without further purification.

Preparation of holey graphene oxide (HGO): Graphene oxide (GO) was prepared from graphite powder by a modified Hummers method reported in our previous study[1]. The holey graphene oxide was synthesized according to a report elsewhere[2]. HGO was prepared according to the following procedure: 50 mL 30% H_2O_2 aqueous solution was added into 500 mL 2 mg/mL GO aqueous dispersion and stirred for 10 minutes to ensure uniform mixing. And then the mixture of graphene oxide and H_2O_2 was heated at 100 °C under stirring for different periods of time to regulate pores on the graphene sheets. The reaction time of the above mixture is 0.5 hours, 1

hour, 1.5 hours and 2 hours, respectively. The unreacted H_2O_2 was removed by centrifuging and washing after the reaction finished to purify the HGO which was finally diluted to 2 mg·mL^{-1}. The reaction for 1.5 hours was optimised to make the HGO in this work.

Synthesis of anisotropic holey graphene aerogel (AHGA): AHGA was synthesized according to the following procedure: first of all, a certain amount of VC was added into a HGO suspension and then stirred for 5 min to obtain a homogeneous dispersion. The mass ratio of VC to HGO is 5 in dispersion. Liquid crystalline HGO was prepared by centrifugation of the above dispersion at a high speed (12000 rpm) for about 1 hour. The resulting HGO liquid crystal (20 mg·mL^{-1}) was loaded into a syringe (diameter: ~1 cm) and was driven by more shearing *via* moving the piston back and forth in order to achieve a more uniform alignment. And then the syringe was annealed in a 30 $^{\circ}$C water bath for 72 hours. HGO hydrogel was obtained after the aging process and then washed by deionized water to remove any hydrosoluble impurities. After that the hydrogel was washed with ethanol *via* solvent exchange to remove various impurities, and then supercritical CO_2 drying was applied to obtain a corresponding aerogel. Finally, the above aerogel was placed into a tube furnace, heated to 900 $^{\circ}$C with a heating rate of 10 $^{\circ}$C /min under an argon flow (200 cm^3/min) and carbonized for 3 hours to obtain an anisotropic holey graphene aerogel. The resulting aerogel is named AHGA-Z, where AHGA is the abbreviation of the anisotropic holey graphene aerogel and Z represents the oxidation time of graphene oxide in H_2O_2. As control experiments, holey graphene aerogel (HGA) and graphene aerogel (GA) were prepared from HGO and GO aqueous suspensions according to the report in our previous study. Anisotropic graphene aerogel (AGA) was obtained from a GO aqueous solution by the same method as described above.

Characterization and measurements: The morphology of the samples was characterized by a scanning electron microscope (SEM) (S-4800) operated at 10 kV and a transmission electron microscope (TEM, Tecnai G2 F20 S-Twin) operated at 200 KV. The pore structure of the aerogels was investigated using a Surface Area Analyzer (Micrometrics, ASAP 2020 HD88). The Brunauer–Emmett–Teller (BET) method and the Barrett–Joyner–Halenda (BJH) model were utilized to calculate the BET specific surface area (SSA) and the pore size distribution. The crystal structure of the as-prepared samples was investigated by X-Ray Diffraction (XRD, D8 advance, Bruker AXS). Raman spectra were recorded using a LabRAM HR Raman Spectrometer (LabRAM HR, Horiba-JY) fitted with a 632.8 nm laser. The compressive stress–strain measurements were performed by using an Instron 3365 tensile testing machine at a crosshead speed of 2 mm·min^{-1}. For the axial compresssion, the cylinder samples were compressed directly; for the radial compress, cube specimens cut from the cylinder samples were tested. The electrical conductivity of the samples with a rectangle length and width of not less than 20 mm were measured by a digital multi-function four-probe tester (Suzhou Jingge Electronic Co., LTD, ST-2258A). The electrochemical performances were measured by an electrochemical workstation (Wuhan Corrtest Instruments Co., Ltd. Wuhan, CS120) with a three-electrode configuration. A piece of aerogel sample (diameter 7.1 mm) was directly pressed into   nickel foam with a load of 7 MPa to serve as the working electrode, a platinum wire was used as the counter electrode, saturated calomel electrode as the reference electrode and 0.1 M NaCl solution containing 0.01M ferro/ferricyanide solution   as the supporting electrolyte. Electrochemical impedance measurements were conducted in the frequency range between 10 kHz and 50 mHz using a commercial instrument (Dual Electrochemical workstation, ZIVE BP2).

17

0.4 M $K_3[Fe(CN)_6]$/$K_3[Fe(CN)_6]$ solution was used as the electrolyte. Platinum and Ag/AgCl electrodes were used as counter and reference electrodes for the electrochemical impedance measurements. A homemade electro-thermal cell was set up to evaluate the electro-thermal performance. Aerogel samples directly pressed into nickel foam with a load of 7 MPa were used as the working electrode and counter electrode, respectively, 0.4 M $K_3[Fe(CN)_6]$/$K_3[Fe(CN)_6]$ was used as the supporting electrolyte, heat band (Omega Engineering China, FGR-030/240V) and circulating water were used to keep the temperature difference. Thermocouple (Fluke, 54ПВ thermometer) was used to monitor the temperature of each electrode.

Supporting Information

Supporting Information is available from the Wiley Online Library or from the author.

References

[1] J. J. Mao, J. Iocozzia, J. Y. Huang, K. Meng, Y. K. Lai, Z. Q. Lin, *Energy Environ. Sci.* **2018**, *11*, 772.

[2] A. I. Hochbaum, R. K. Chen, R. D. Delgado, W. J. Liang, E. C. Garnett, M. Najarian, A. Majumdar, P. D. Yang, *Nature* **2008**, *451*, 163.

[3] J. S. Rhyee, K. H. Lee, S. M. Lee, E. Cho, S. Il Kim, E. Lee, Y. S. Kwon, J. H. Shim, G. Kotliar, *Nature* **2009**, *459*, 965.

[4] L. E. Bell, *Science* **2008**, *321*, 1457.

[5] a) K. L. Peng, X. Lu, H. Zhan, S. Hui, X. D. Tang, G. W. Wang, J. Y. Dai, C. Uher, G. Y. Wang, X. Y. Zhou, *Energy Environ. Sci.* **2016**, *9*, 454; b) C. Sealy, *Nano Today* **2010**, *5*, 163; c) L. D. Zhao, J. Q. He, D. Berardan, Y. H. Lin, J. F. Li, C. W. Nan, N. Dragoe, *Energy Environ. Sci.* **2014**, *7*, 2900; d) M. Zhao, J. Zhang, N. Y. Gao, P. Song, M. Bosman, B. Peng, B. Q. Sun, C. W. Qiu, Q. H. Xu, Q. L. Bao, K. P. Loh, *Adv. Mater.* **2016**, *28*, 3138.

[6] a) D. P. Dong, H. T. Guo, G. Y. Li, L. F. Yan, X. T. Zhang, W. H. Song, *Nano Energy* **2017**, *39*, 470; b) T. J. Kang, S. Fang, M. E. Kozlov, C. S. Haines, L. Na, H. K. Yong, Y. Chen, R. H. Baughman, *Adv. Funct. Mater.* **2012**, *22*, 477; c) M. F. Dupont, D. R. MacFarlane, J. M. Pringle, *Chem. Commun.* **2017**, *53*, 6288.

[7] T. J. Abraham, D. Macfarlane, J. M. Pringle, *Energy Environ. Sci.* **2013**, *6*, 2639.

[8] a) E. L. Smith, A. P. Abbott, K. S. Ryder, *Chem. Rev.* **2014**, *114*, 11060; b) Q. H. Zhang, K. D. Vigier, S. Royer, F. Jerome, *Chem. Soc. Rev.* **2012**, *41*, 7108; c) Y. Gao, Z. Qin, L. Guan, X. Wang, G. Z. Chen, *Chem. Commun.* **2015**, *51*, 10819; d) T. I. Quickenden, Y. Mua, *J. Electrochem. Soc.* **1996**, *27*, 3985.

[9] P. F. Salazar, S. Kumar, B. A. Cola, *J. Appl. Electrochem.* **2014**, *44*, 325.

[10] Z. Li, Z. Liu, H. Sun, C. Gao, *Chem. Rev.* **2015**, *115*, 7046.

[11] X. Zhang, Z. Sui, B. Xu, S. Yue, Y. Luo, W. Zhan, B. Liu, *J. Mater. Chem.* **2011**, *21*, 6494.

[12] a) Z. Xu, C. Gao, *ACS Nano* **2011**, *5*, 2908; b) Z. Liu, Z. Li, Z. Xu, Z. Xia, X. Hu, L. Kou, L. Peng, Y. Wie, C. Gao, *Chem. Mater.* **2014**, *26*, 6786; c) Z. Xu, Y. Zhang, P. G. Li, C. Gao, *ACS Nano* **2012**, *6*, 7103.

[13] a) W. H. Song, H. Tu, G. Goldbeck-Wood, A. H. Windle, *J. Phys. Chem.* **2005**, *109*, 19234; b) W. H. Song, I. Kinloch, A.H. Windle, *Science*, **2003**, *302*, 1363; c) W. H. Song, A. H. Windle, *Adv. Mater*. **2008**, *20*, 3149.

[14] a) G. Li, X. Zhang, W. Jin, J. Fang, *J. Mater. Chem. A* **2016**, *4*, 17042; b) H. Yang, Z. Li, B. Lu, J. Gao, X. Jin, G. Sun, G. Zhang, P. Zhang, L. Qu, *ACS Nano*.**2018**, *12*, 11407.

[15] W. Song, S. Chen, Y. Jin and R. Qian, *Liq. Cryst.* **1995**, *19*, 549.

[16] a) H. T. Sun, L. Mei, J. F. Liang, Z. P. Zhao, C. Lee, H. L. Fei, M. N. Ding, J. Lau, M. F. Li, C. Wang, X. Xu, G. L. Hao, B. Papandrea, I. Shakir, B. Dunn, Y. Huang, X. F. Duan, *Science* **2017**, *356*, 599; b) Y. X. Xu, C. Y. Chen, Z. P. Zhao, Z. Y. Lin, C. Lee, X. Xu, C. Wang, Y. Huang, M. I. Shakir, X. F. Duan, *Nano Lett.* **2015**, *15*, 4605.

[17] L. Qiu, L. D. Li, H. Cheng, *ACS Nano* **2018**, *12*, 5085.

[18] a) H. Huang, P. Chen, X. Zhang, Y. Lu, W. Zhan, *Small* **2013**, *9*, 1397; b) M. Yang, N. Zhao, Y. Cui, W. Gao, Q. Zhao, C. Gao, H. Bai, T. Xie, *ACS Nano* **2017**, *11*, 6817; c) C. Wang, X. Chen, B. Wang, M. Huang, B. Wang, Y. Jiang, R. S. Ruoff, *ACS Nano* **2018**, *12*, 5816; d) J. Kim, N. M. Han, J. Kim, J. Lee, J. K. Kim, S. Jeon, *ACS Appl. Mater. Interfaces* **2018**, *10*, 37507.

[19] T. Kim, J. S. Lee, G. Lee, H. Yoon, J. Yoon, T. J. Kang, H. K. Yong, *Nano Energy* **2017**, *31*, 160.

[20] X. M. Zhang, M. Kar, T. C. Mendes, Y. T. Wu, D. R. MacFarlane, *Adv. Energy Mater.* **2018**, *8*, 1702702.

[21] Q. W. Yang, Z. Q. Zhang, X. G. Sun, Y. S. Hu, H. B. Xing, S. Dai, *Chem. Soc. Rev.* **2018**, *47*, 2020.

[22] T. Migita, N. Tachikawa, Y. Katayama, T. Miura, *Electrochemistry* **2009**, *77*, 639.

[23] R. J. Mehta, Y. L. Zhang, H. Zhu, D. S. Parker, M. Belley, D. J. Singh, R. Ramprasad, T. Borca-Tasciuc, G. Ramanath, *Nano Lett.* **2012**, *12*, 4523.

[24] H. Im, T. Kim, H. Song, J. Choi, J. S. Park, R. Ovalle-Robles, H. D. Yang, K. D. Kihm, R. H. Baughman, H. H. Lee, T. J. Kang, Y. H. Kim, *Nat. Commun.* **2016**, *7*, 10600.

[25] L. Lu, M. Zhang, X. Zhang, Z. Zhang, *J. Power Sources* **2017**, *364*, 234.

[26] M. S. Romano, N. Li, D. Antiohos, J. M. Razal, A. Nattestad, S. Beirne, S. Fang, Y. Chen, R. Jalili, G. G. Wallace, *Adv. Mater.* **2013**, *25*, 6602.

[27] L. Zhang, T. Kim, N. Li, T. J. Kang, J. Chen, J. M. Pringle, M. Zhang, A. H. Kazimv, S. Fang, C. Haines, D. Al-Masri, B. A. Cola, J. M. Razal, J. Di, S. Beirne, D. R. MacFarlane, A.

Gonzalez-Martin, S. Mathew, Y. H. Kim, G. Wallace, R. H. Baughman, *Adv. Mater.* **2017**, *29*, 1605652.

[28] S. H. Kim, C. S. Haines, N. Li, K. J. Kim, T. J. Mun, C. Choi, J. T. Di, Y. J. Oh, J. P. Oviedo, J. Bykova, S. L. Fang, N. Jiang, Z. F. Liu, R. Wang, P. Kumar, R. Qiao, S. Priya, K. Cho, M. Kim, M. S. Lucas, L. F. Drummy, B. Maruyama, D. Y. Lee, X. Lepro, E. L. Gao, D. Albarq, R. Ovalle-Robles, S. J. Kim, R. H. Baughman, *Science* **2017**, *357*, 773.

[29] F. Zhao, Y. Liang, H. H. Cheng, L. Jiang, L. T. Qu, *Energy Environ. Sci.* **2016**, *9*, 912.

[30] I. Hyeongwook, M. Hyung Geun, L. Jeong Seok, C. In Young, K. Tae June, K. Yong Hyup, *Nano Res.* **2014**, *7*, 443.

[31] P. Yang, K. Liu, Q. Chen, X. Mo, Y. Zhou, S. Li, G. Feng, J. Zhou, *Angew. Chem. Int. Ed.* **2016**, *55*, 12050.
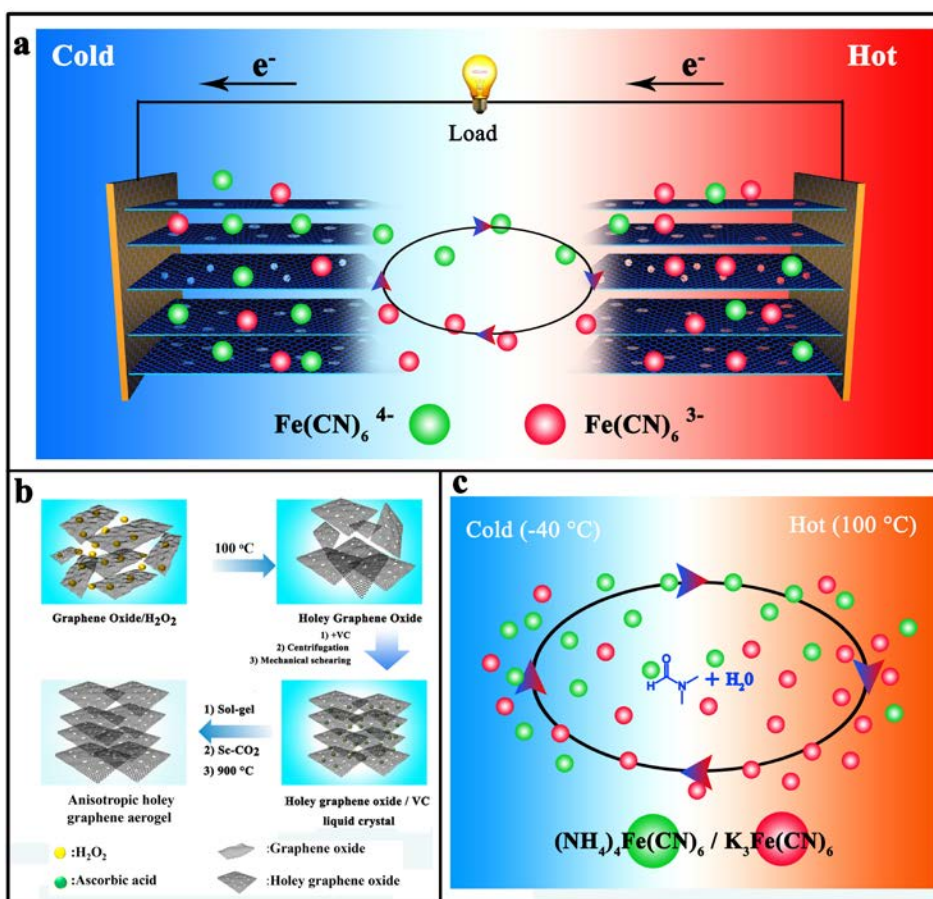
Figure 1. Schematic mechanism of an electrochemical thermocell based on anisotropic holey graphene aerogel (AHGA) electrodes. (a) The schematic of an electrochemical thermocell based on anisotropic holey graphene aerogel electrodes. (b) Synthesis of the AHGA. (c) The schematic of a low-temperature electrolyte of a eutectic mixture of potassium ferricyanide and potassium ferrocyanide in a formamide and water mixed solvent.
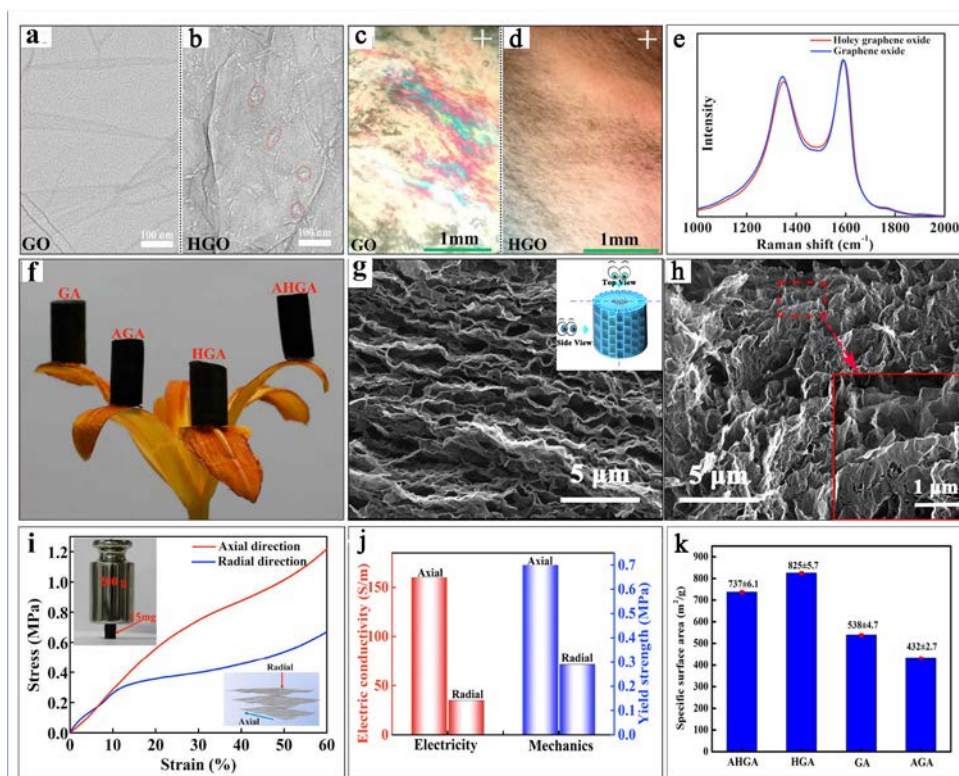
Figure 2. a,b) TEM images of graphene oxide (a) and holey graphene oxide (b). c,d) The optical texture of graphene oxide liquid crystal (c) and holey graphene oxide liquid crystal (d) under a corss-polarized-light optical microscope (POM); (e) Raman spectra of graphene oxide and holey graphene oxide; (f) a digital photo of cylinders of graphene aerogel (GA), anisotropic graphene aerogel (AGA), holey graphene aerogel (HGA), anisotropic holey graphene aerogel (AHGA) support by a lily flower petals; (g-h) SEM images of the facture surfaces of perpendicular (g, top view) and parallel (h, side view) to the long axis of AHGA cylinder. The inset in (g) is the illustration direction of AHGA cylinder. (i) Compressive stress–strain curves measured from the cubic samples. The inset in (i) is a 15 mg anisotropic holey graphene aerogel cylinder supporting a 200 g counterpoise, more than 13000 times of its own weight. (j) Conductivity and mechanical strength of the anisotropic holey graphene aerogel in different directions; (k) specific surface area of the different aerogels.
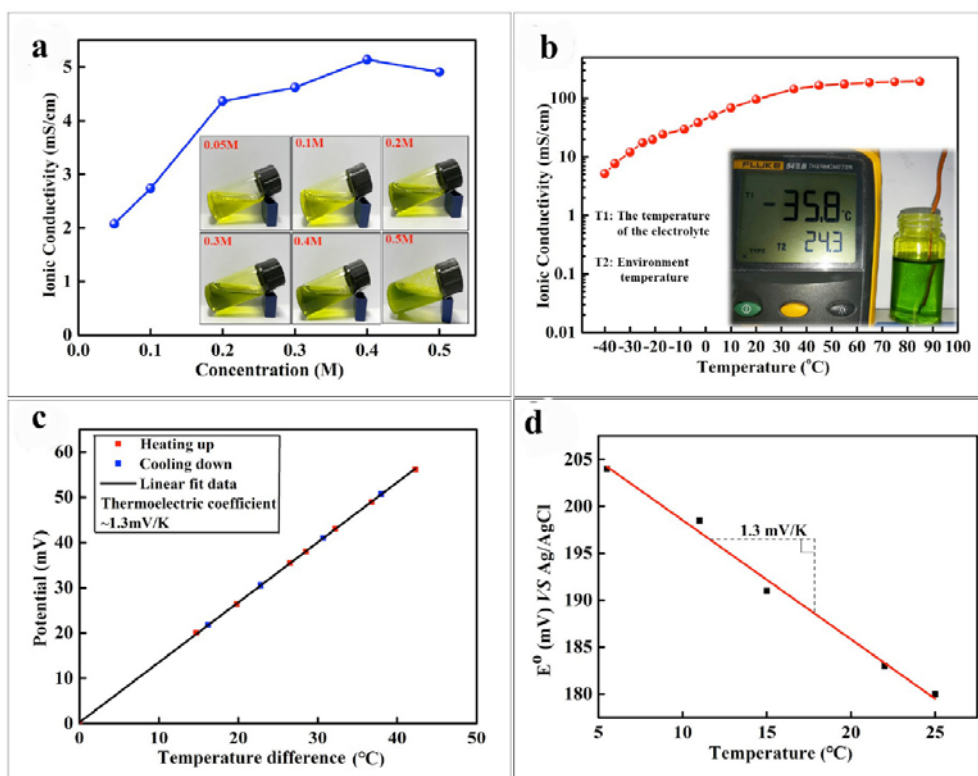
Figure 3. (a) Conductivity of the electrolyte with different concentrations at minus 40 °C, the inset is the photographs of the electrolyte with different concentrations after being placed at minus 40 °C for half an hour, (b) Conductivity of 0.4 M electrolyte at different temperatures, the inset is a photo of the test of electrolyte temperature by thermocouple, (c) Seebeck coefficient of the 0.4 M $Fe(CN)_6^{4-}/Fe(CN)_6^{3-}$ electrolyte and (d) Formal potential of 1.0 mM $Fe(CN)_6^{3-}$ electrolyte as a function of temperature.
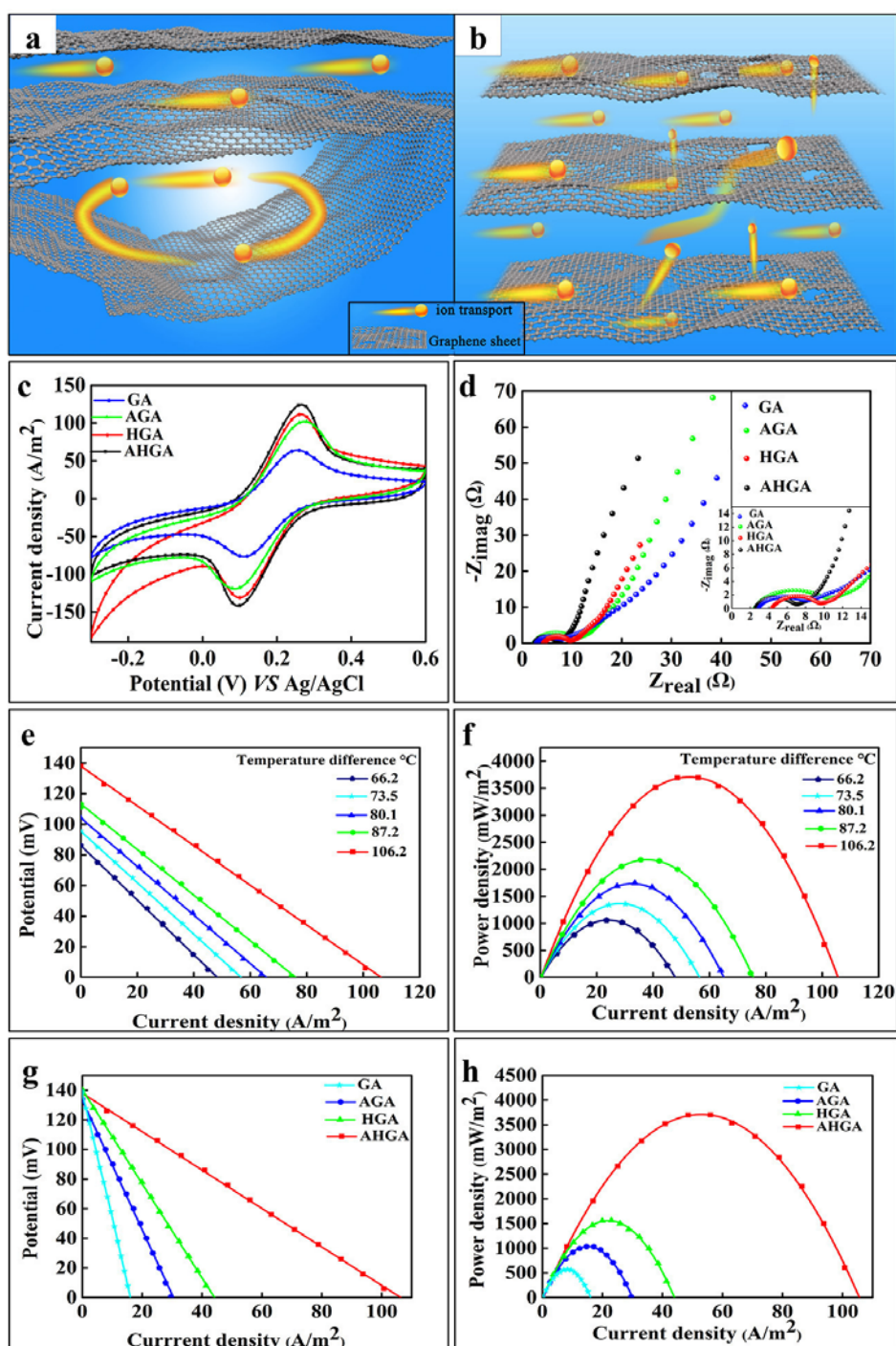
Figure 4. Ionic transport model in (a) random graphene channels and (b) ordered holey graphene channels; (c) CV curves and (d) electrochemical impedance spectra of different electrode materials; (e) output potential and (f) output power of the anisotropic graphene aerogel electrode with various temperature differences; (g) output potential and (h) output power of the thermocell with different electrode materials between −40 ℃ and 100 ℃
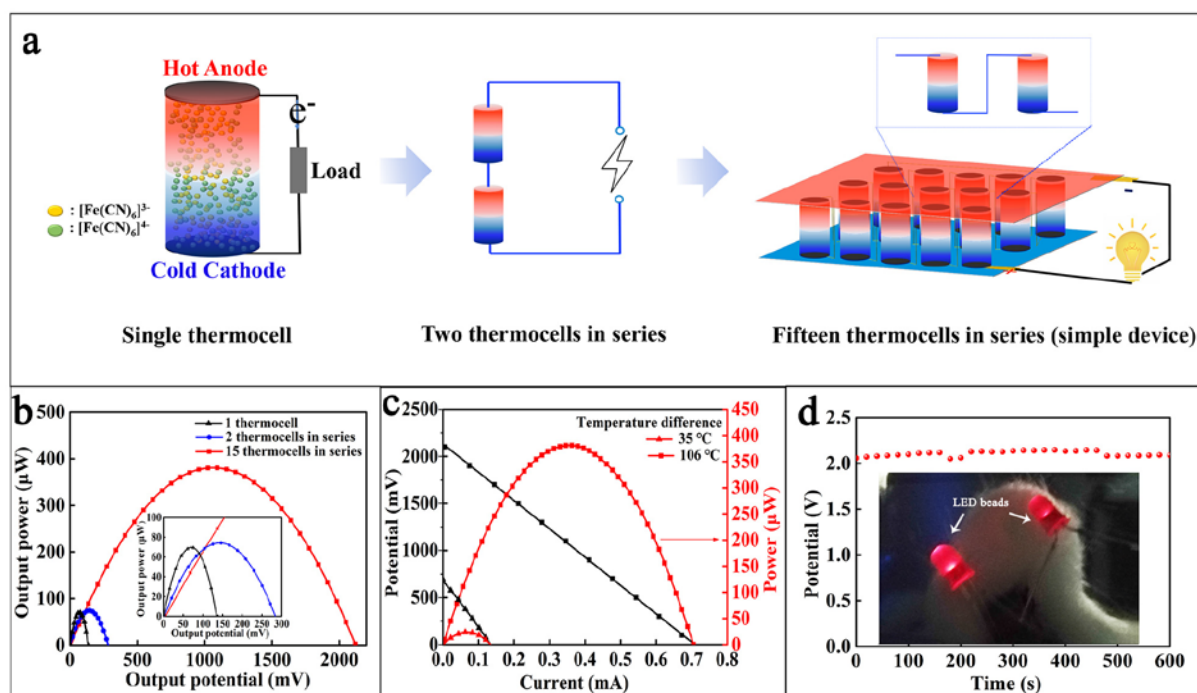
Figure 5. (a) Schematic diagram of a single thermocell, 2-cylinder thermocells in series and a low-temperature thermocell device; (b) plots of the output power versus the output voltage of the single thermocell, 2-cylinder thermocells in series and 15-cylinder low-temperature thermocell device tested between -40 °C and 100 °C; (c) plots of the output voltage and the power versus the current of the 15-cylinder device with different temperature differences. The output voltage versus time obtained from ΔT= 106 °C (d). The inset in (d) is the photo of the LED beads lighted by the device

TOC

The highly efficient cylindrical cryo-thermocells, working in a wide operation window of cold temperatures, have been developed via the combination of anisotropic holey graphene aerogel electrodes and a eutectic redox electrolyte.

Keyword: cryo-thermocells, anisotropyic graphene aerogel, holey graphene, eutectic redox electrolyte

Guangyong Li,[†], Dapeng Dong[†], Guo Hong[†], Lifeng Yan, Xuetong Zhang*, Wenhui Song*

High-efficiency cryo-thermocells assembled with anisotropic holey graphene aerogel electrodes and a eutectic redox electrolyte

ToC figure ((Please choose one size: 55 mm broad × 50 mm high **or** 110 mm broad × 20 mm high. Please do not use any other dimensions))
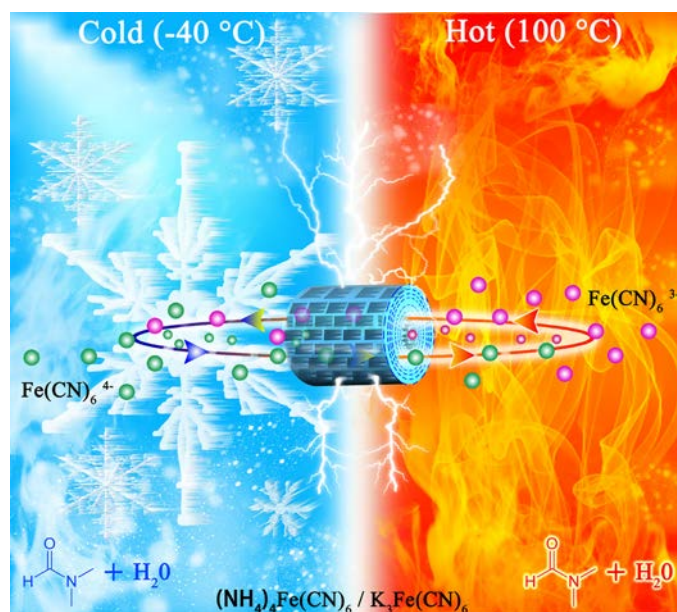
Supporting Information

High-efficiency cryo-thermocells assembled with anisotropic holey graphene aerogel electrodes and a eutectic redox electrolyte

Guangyong Li[†]*, Dapeng Dong*[†]*, Guo Hong*[†]*, Lifeng Yan, Xuetong Zhang*, Wenhui Song**

Method

For a hypothetical redox reaction in thermocell system, $B = ne^- + A$, such as：

Cold electrode: $Fe(CN)_6^{4-} - e^- = Fe(CN)_6^{3-}$

Hot electrode: $Fe(CN)_6^{3-} + e^- = Fe(CN)_6^{4-}$　　　　　　　　　(1)
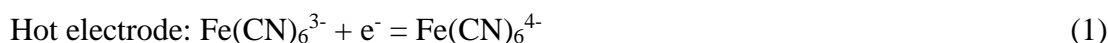
Above reactions show that oxidation occurs at the hot electrode and reduction at the cold electrode. The oxidation of ferrocyanide allows the extraction of electrons at the anode. These electrons travel through an external circuit and are consumed at the cathode through the reduction of ferricyanide. Diffusion and convection facilitate the mass transport needed to prevent accumulation of reaction products at either half-cell allowing thermocells to operate in a self-sustaining manner.

The thermoelectric coefficient can be expressed as:[3]

$S = \partial v/\partial T = \Delta S_{B,A}/nF$　　　　　　　　　　　(2)

where T is the temperature, v is the electrode potential, n is the number of electrons involved in the reaction, F is Faraday's constant, and $\Delta S_{B,A}$ is the reaction entropy for the redox couple, respectively. By rearranging Eq. (2), the open circuit voltage (V_{oc}) of the

thermocell is dictated by the reaction entropy of the redox couple ($\Delta S_{B,A}$) and the temperature difference (ΔT) to which the half-cells are exposed to as shown in Eq. (3).[3]

$$V_{oc} = (\Delta T \Delta S_{B,A})/nF \tag{3}$$

Therefore, the output potential of the thermocell is proportional to the temperature difference between the heat source and the heat sink. Also, the temperature difference determines the maximum electrical output power of the thermocell as[3]:

$$P_{max} = 0.25 V_{oc} I_{sc} \tag{4}$$

where P_{max} is the maximum power, which occurs when the external load resistance is set equal to the internal resistance of the cell. P_{max} in Equation 4 can be obtained from experimental characteristic curves of potential difference, E, versus current, I. In the simplest case, in which such E–I curves are linear, it is easy to show that P_{max} is given by the rectangle of greatest area under the E–I curve. V_{oc} is the open circuit voltage and I_{sc} is the short circuit current, which delivered by thermocell. As a result, the power density of the thermocell is determined by the temperature difference (ΔT) and ion conductivity of the electrode, which dominates the short circuit current.

The power conversion efficiency (η) and relative power conversion efficiency (η_r) was described as blew:

$$\eta = (0.25\ V_{oc}*I_{sc})/(A\kappa(\Delta T/d)) = P_{max}/(A\kappa(\Delta T/d)) \tag{5}$$

$$\eta_r = \eta/(\Delta T/T_h) \tag{6}$$

where A is the cross-sectional area of the electrode, κ respires the thermal conductivity of the redox couple, ΔT the temperature difference, d the distance between two test electrodes, η the power conversion efficiency, T_h the temperature of the hot side, V_{oc} the open circuit potentials and I_{sc} the shorting circuit current.

Figures
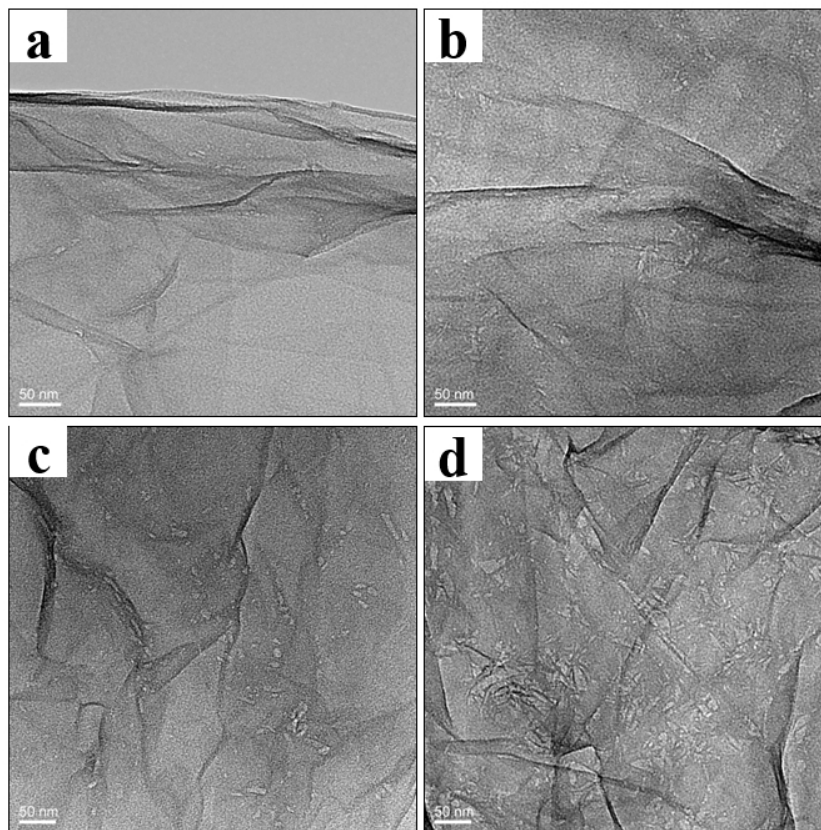
Figure S1 TEM images of HGO with different etching time, (a) 0.5h (b) 1h (c) 1.5h (d) 2h.

Figure S2 POM images of GO and HGO with different etching time. As the etching time increasing, the POM image of HGO exhibited less colorful textile.

Figure S3 POM image of the mixture of the holey graphene oxide and Vitamin C
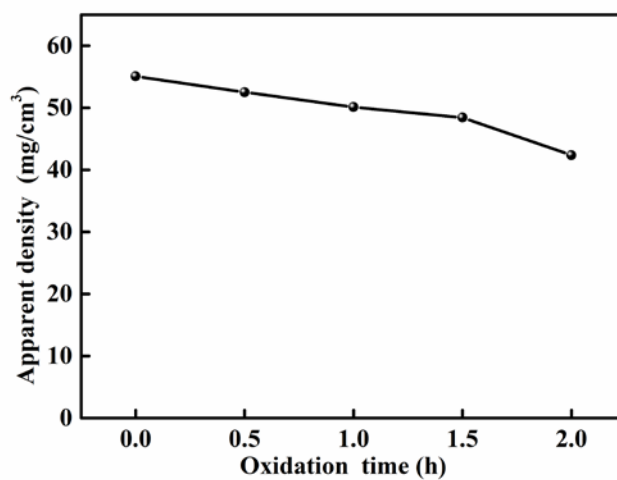
Figure S4 The relationship between the apparent density of aerogel assembled by holey graphene oxide with different etching time.
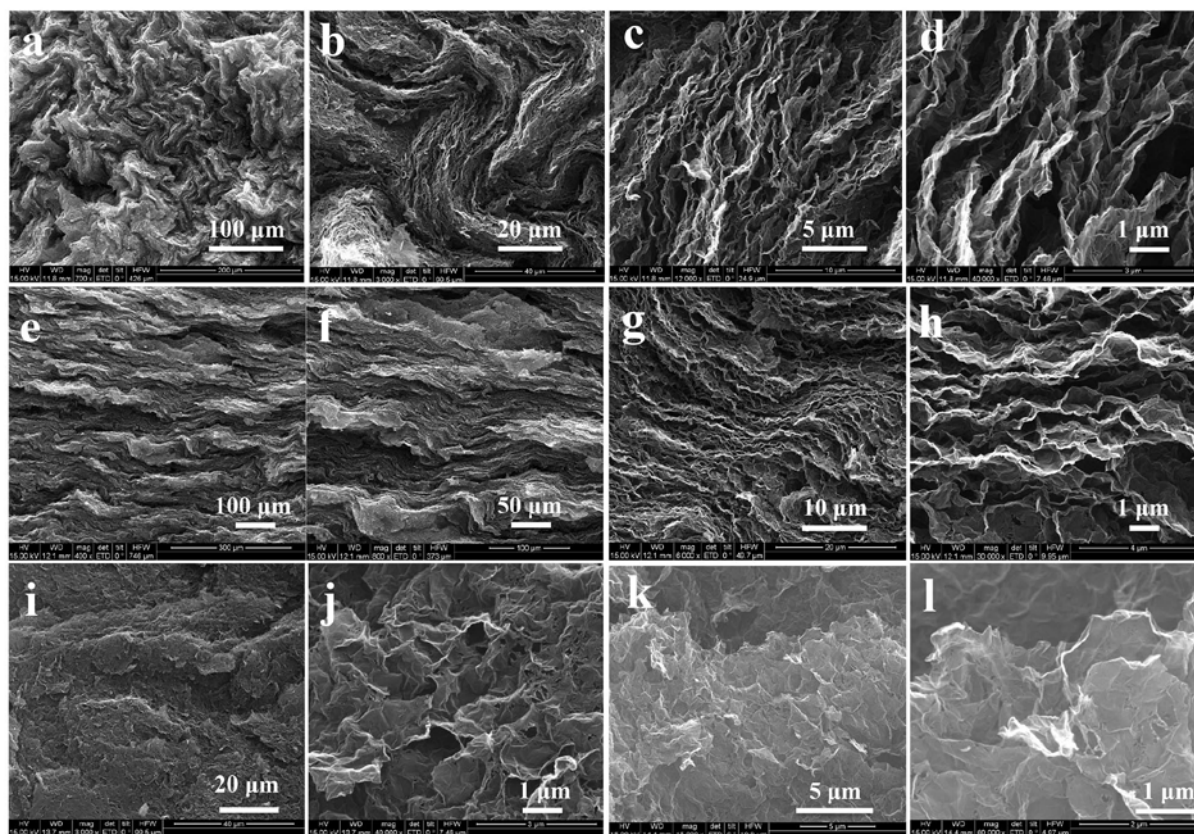
Figure S5 SEM images of the facture surfaces of the perpendicular (a-h) and parallel (i-l) of AHGA cylinder long axis.
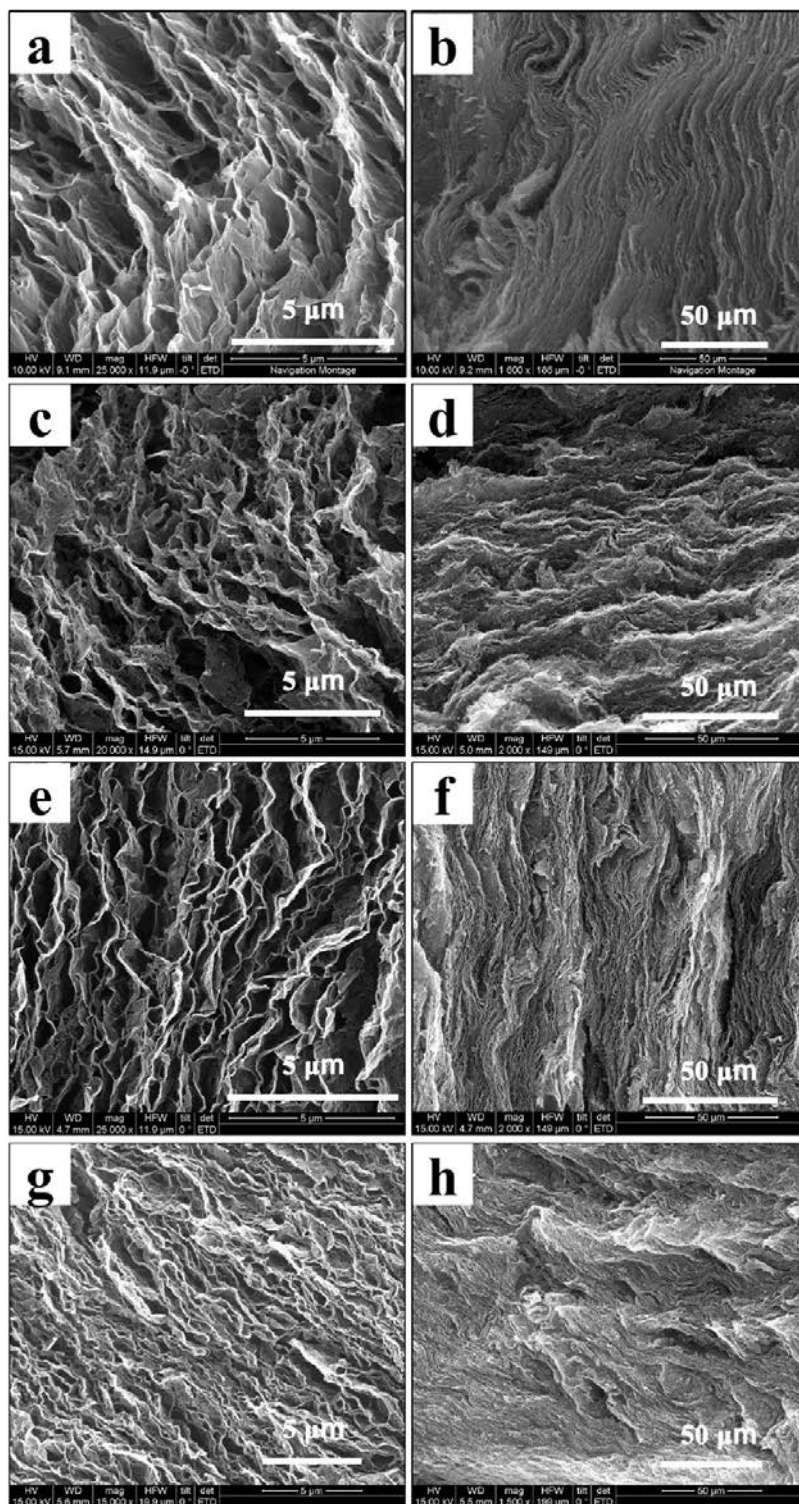
Figure S6 SEM images of the facture surfaces of the perpendicular of AHGA cylinder long axis. (a-b) graphene oxide. (c-h) holey graphene oxide obtained after oxidation for 0.5 hour (c-d), 1 hour (e-f), 1.5hours (g-h) with hydrogen peroxide.
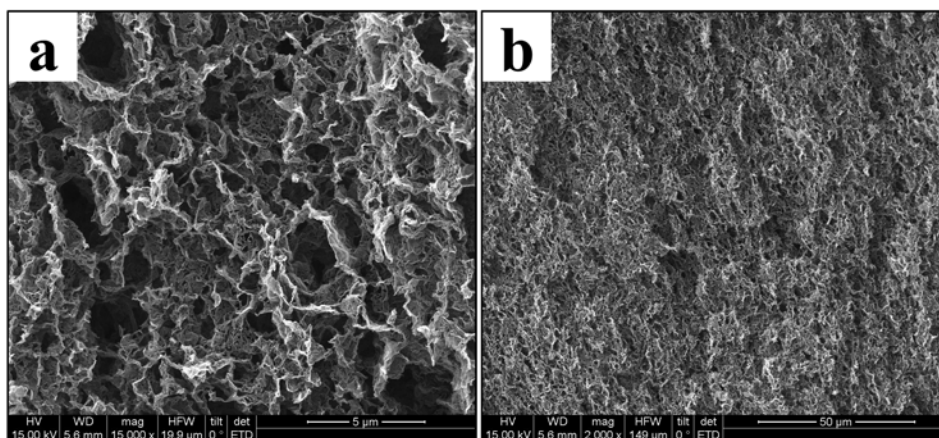
Figure S7 SEM images of holey graphene aerogel assembled from holey graphene oxide treated by hydrogen peroxide for two hours
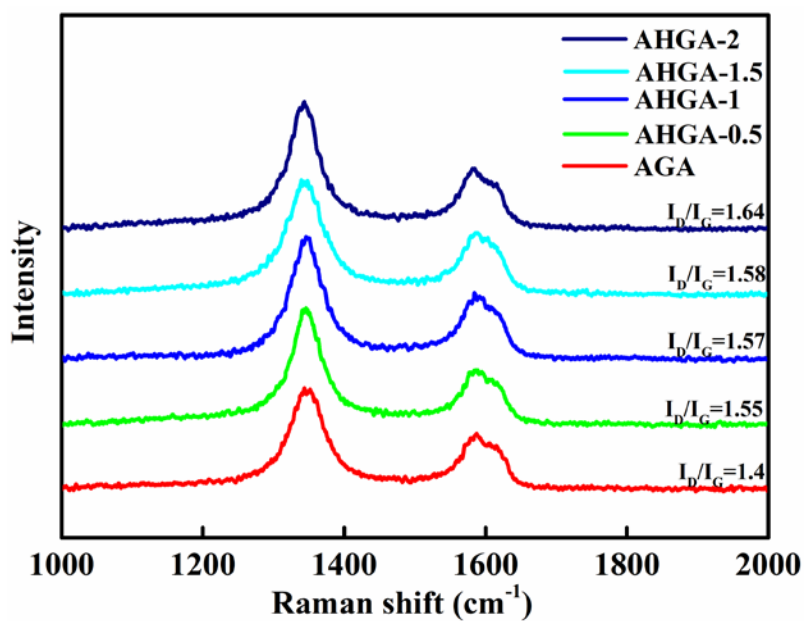
Figure S8 Raman spectrum of the aerogels assembled from graphene oxide and holey graphene oxide obtained after oxidation for different time with hydrogen peroxide. Defects on the graphene sheet increased with the etching time.
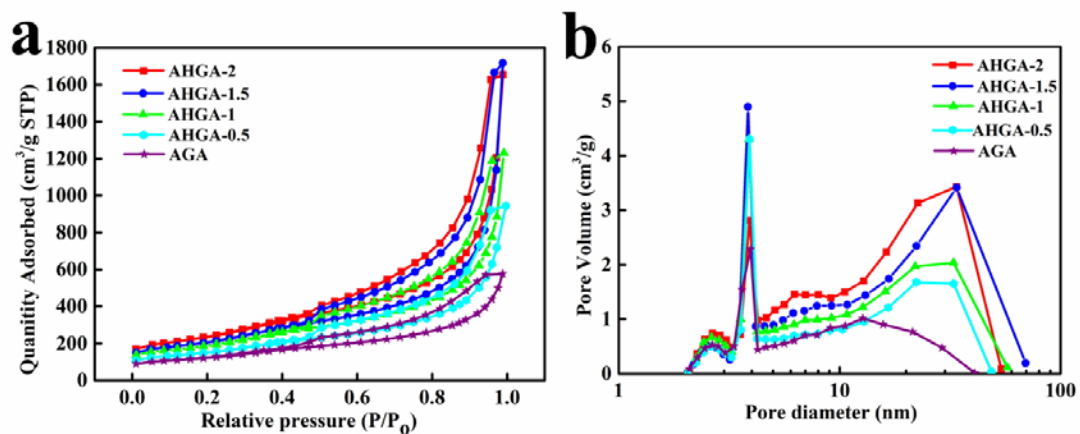
Figure S9 (a) N$_2$ sorption isotherm curves and (b) pore-size distribution curves of the aerogels assembled from graphene oxide and graphene oxide and holey graphene oxide obtained after oxidation for different time with hydrogen peroxide
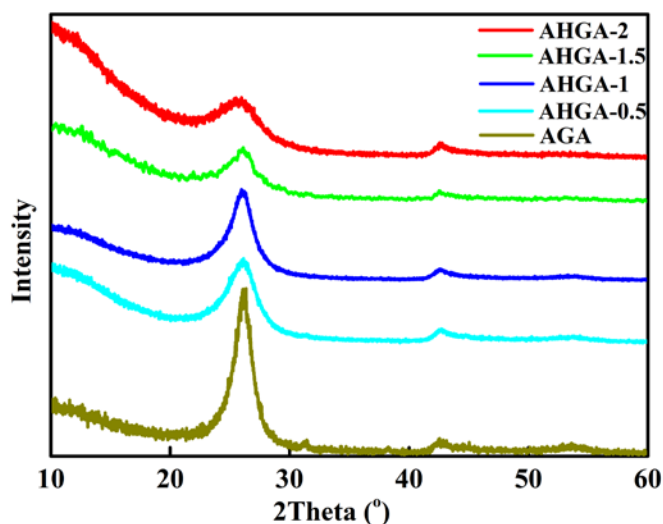
Figure S10 XRD pattern of the aerogels assembled from graphene oxide and holey graphene

oxide obtained after oxidation for different time with hydrogen peroxide.

AHGA show a 0.5 degree blue shift compared to the anisotropic graphene aerogel at the (001)

diffraction peak Those results show that the spacing of holey graphene sheets in AHGA is

larger than the spacing of graphene sheets in anisotropic graphene aerogels, which proves that

the holey graphene oxide has larger sheet wrinkles than the untreated graphene oxide, thereby

effectively preventing excessive stacking of the graphene sheets.
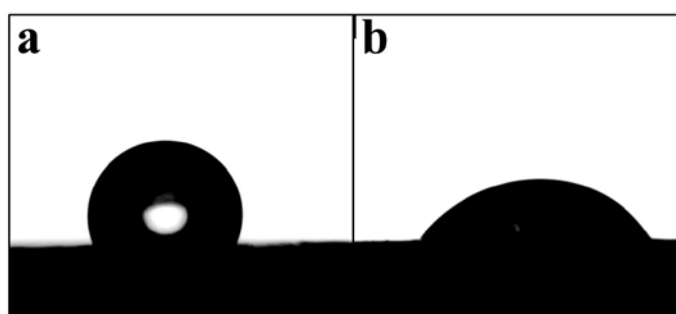
Figure S11 Contact angle of 0.4M (a) aqueous electrolyte solution and (b) organoaqueous

electrolyte solutions on anisotropic holey graphene aerogel electrode is 116.7º and 55º, which

means that the organoaqueous electrolyte has better wettability to the electrode material.
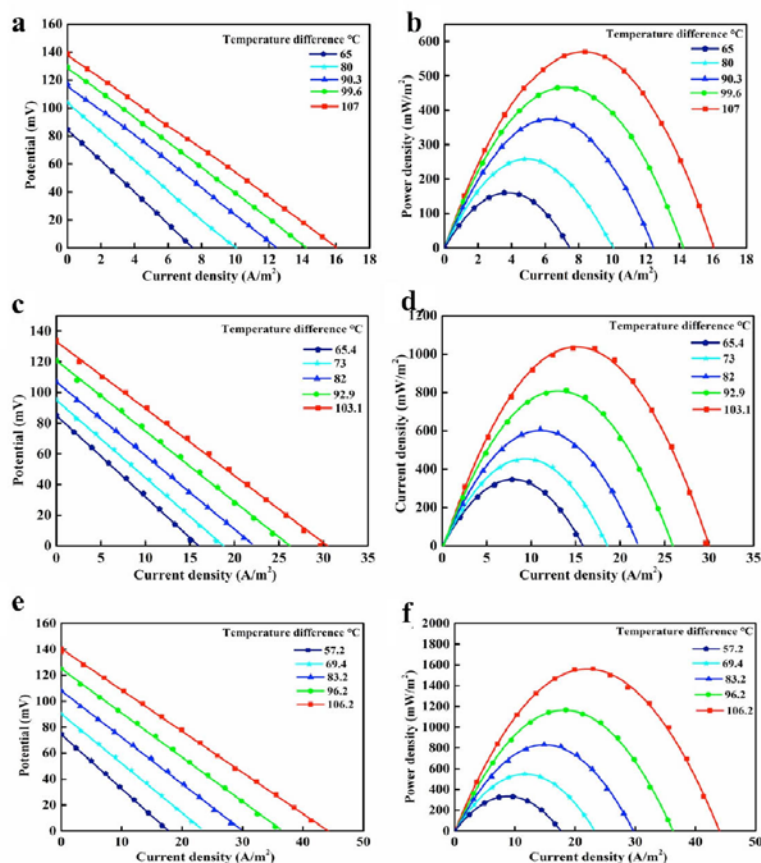
Figure S12 Output potential and output power density of (a, b) graphene aerogel electrode, (c, d) anisotropic graphene aerogel electrode and (e, f) anisotropic holey graphene aerogel electrode with various temperature difference.

As control experiments, different aerogels were selected as electrode materials to assemble individual thermocell columns, and then their thermoelectric properties were tested under different temperature differences. The graphene aerogel electrode with disordered pore structure has the worst performance because of its large ion transport resistance. The performance of anisotropic graphene aerogel electrodes is superior to graphene aerogels because their ordered pore structure can reduce ion transport resistance. The holey graphene aerogel electrode has better performance because the introduction of pores on the graphene increases the ion transport channel and increases the specific surface area.
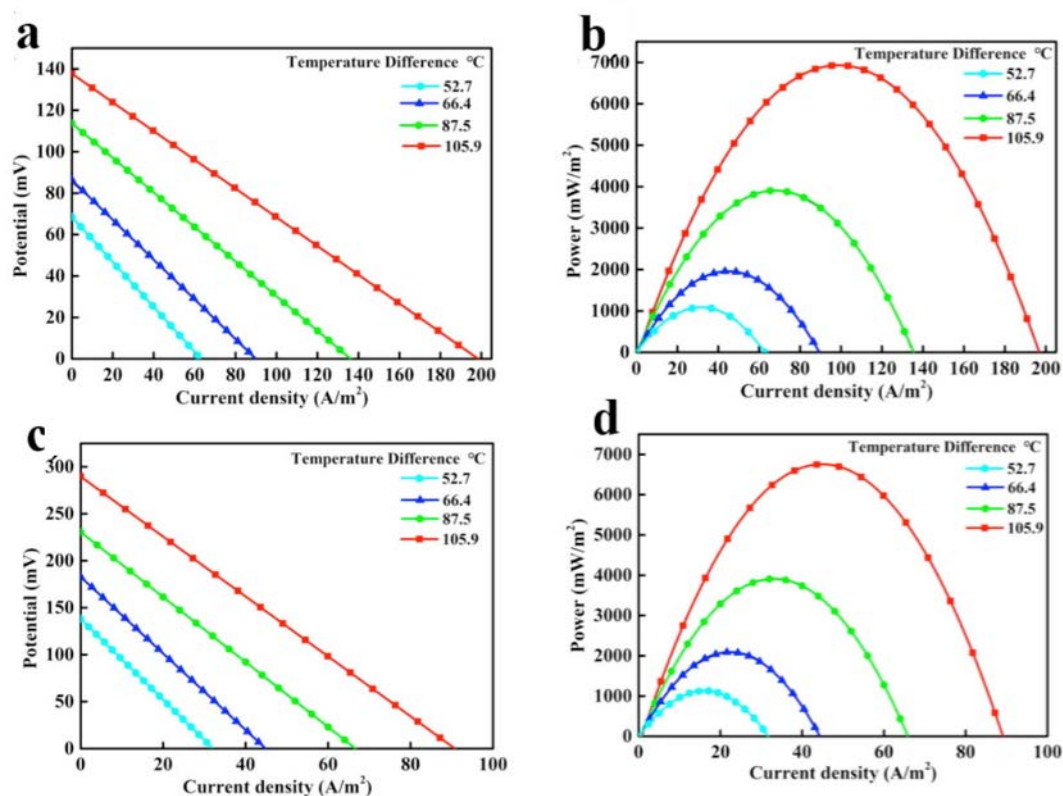
Figure S13 Performance of two thermocells (a) and (b) in parallel, and (c) and (d) in series with different temperature difference.

In order to investigate the integrability of the single thermocell column, the output signals of two thermocells were measured in both parallel and series connections. As shown in Figure S13 (a), the current density generated by two thermocells connected in parallel reached 200 A/m^2, which is almost identical to the sum of the current density values for each thermocell separately. On the other hand, as shown in Figure S13(c), the output potential generated by integrating two thermocells connected in series exceeded 280mV, which is similar to that of the sum of the output potential values for each thermocell separately. As a result, regardless which type the two thermocells are connected, the output power density of the assembled thermocells doubled that of a single thermocell, as show in Figure S12 (b) (d).

Figure S14 Photographs of single cryo-thermocell (a), thermocell device (b, 15 in series) and the LED beads (c) were lighted by the thermocell device.

Table S1. Comparison of the thermoelectric property of AHGA-aerogel based thermocell with other nanomaterials or nanocomposites based reported in the literature:

Electrode	Microstructure	Electrolyte (ferro/ferricyanide redox couple)	Seebeck coefficient (mV/K)	Temperature window (temperature difference °C)	P_{max} (Specified)/ W m^{-2}	η_r (%)	Remarks	Reference [3a,4,5]
AHGAs	Aligned pore channel and holy wall	A eutectic electrolyte onsisting of formamide and water	1.3	**106**	3.6	0.7	Cylinder-thermocell	**This work**
Graphene-carbon sphere polylithic aerogels	Disordered porous network	water	1.43	~62	1.05	1.4	U-thermocell	*Nano Energy* **2017**, 39, 470.
Carbon-nanotube	Vertical forests	water	1.4	60	0.76	Not mentioned	Coinlike	*Nano Lett.* **2010**, *10*, 838.
SWCNTs	Disordered porous network	water	1.43	20	0.09	0.275	Tube-thermocell	*Adv. Funct. Mater.* **2012**, *22*, 477.
RGO films	Porous lamellar	water	1.41	60	25.51W/ kg	0.012	U-thermocell	*J. Therm Anal Calorim,* **2012**, *109* 1229
SWNT-rGO composites	Gaps	water	Not mentioned	31	0.327W/ m^2	0.64	Tube-thermocell	*Adv. Mater.* **2013**, *25*, 6602–6606
activated carbon textile coated with carbon nanotubes	Textile	water	1.4	3.4	0.46mW /m^2	Not mentioned	Plate-thermocell	*Nano Research.* **2014**, *7*, 443–452
Ag–MgO–CNTs composites	Disordered porous network	water	1.42	50	0.34 W/m^2	0.6	U-thermocell	*RSC. Adv.* **2015**, *5*, 97982-97 987.
MWNT films	Disordered porous network	water	1.42	40	0.82 W/m^2	0.9	U-thermocell	*Nano-Micro Lett.* **2016**, *8*, 240-246.
forest-drawn CNT sheets	Vertically aligned arrays	water	1.4	51	0.04 W/m^2	Not mentioned	Tube-thermocell	*Nat. commun.,* **2016**, *7*, 10600.
Carbon mutli-walled nanotube foam	Disordered porous network	water	1.43	86	1.2 W/m^2	0.4	Button-thermocell	*Adv. Mater.* **201 7**, *29*, 1605652

Table S2. N$_2$ adsorption data of aerogels assembled by graphene etching with different time

Sample ID	BET (m^2·g^{-1})			Pore volume (cm^3·g^{-1})
	t-Plot micropore area	t-Plot external surface area	BET surface area	
AGA	53.5	378.8	432.3	0.9
AHGA-0.5	46.6	490.9	537.5	1.5
AHGA-1	64.7	608.1	672.8	1.9
AHGA-1.5	60.4	677.1	737.5	2.6
AHGA-2	83.6	754.3	837.9	2.6

Reference:

[1]. a) B. Xu, S. F. Yue, Z. Y. Sui, X. T. Zhang, S. S. Hou, G. P. Cao, Y. S. Yang, *Energy Environ. Sci.* **2011,** *4* 2826-2830. b) H. Huang, P. Chen, X. Zhang, Y. Lu, W. Zhan, *Small* **2013**, *9*, 1397-1404.

[2] Y. X. Xu, C. Y. Chen, Z. P. Zhao, Z. Y. Lin, C. Lee, X. Xu, C. Wang, Y. Huang, M. I. Shakir, X. F. Duan, *Nano Lett.* **2015**, *15*, 4605.

[3] a) P. F. Salazar, S. Kumar, B. A. Cola, *J. Appl. Electrochem.* **2014**, *44*, 325. b)L. Zhang, T. Kim, N. Li, T. J. Kang, J. Chen, J. M. Pringle, M. Zhang, A. H. Kazimv, S. Fang, C. Haines, D. Al-Masri, B. A. Cola, J. M. Razal, J. Di，S. Beirne, D. R. MacFarlane, A. Gonzalez-Martin, S. Mathew, Y. H. Kim, G. Wallace, R. H. Baughman, *Adv. Mater.* **2017**, *29*, 1605652.

[4] T. J. Kang, S. Fang, M. E. Kozlov, C. S. Haines, N. Li, H. K. Yong, Y. Chen, R. H. Baughman, *Adv. Funct. Mater*. **2012**, *22*, 477.

[5] a) D. P. Dong, H. T. Guo, G. Y. Li, L. F. Yan, X. T. Zhang, W. H. Song, *Nano Energy* **2017**, 39, 470; b) R. Hu, B. A. Cola, N. Haram, J. N. Barisci, S. Lee, S. Stoughton, G. Wallace, C. Too, M. Thomas, A. Gestos, *Nano Lett.* **2010**, *10*, 838; c) M. S. Romano, S. Gambhir, J. M. Razal, A. Gestos, G. G. Wallace, J. Chen, *J. Therm. Anal. Calorim.* **2012**, *109*, 1229; d) M. S. Romano, N. Li, D. Antiohos, J. M. Razal, A. Nattestad, S. Beirne, S. Fang, Y. Chen, R. Jalili, G. G. Wallace, *Adv. Mater.* **2013**, *25*, 6602; e) I. Hyeongwook, M. Hyung Geun, L. Jeong Seok, C. In Young, K. Tae June, K. Yong Hyup, *Nano resarch* **2014**, *7*, 443; f) W. Qian, M. Li, L. Chen, J. Zhang, C. Dong, *Rsc Adv.* **2015**, *5*, 97982; g) W. Qian, M. Cao, F. Xie, C. Dong, *Nano-Micro Lett.* **2016**, *8*, 240; h) H. Im, T. Kim, H. Song, J. Choi, J. S. Park, R. Ovalle-Robles, H. D. Yang, K. D. Kihm, R. H. Baughman, H. H. Lee, T. J. Kang, Y. H. Kim, *Nature Comm.* **2016**, 7, 10600; i) L. Zhang, T. Kim, N. Li, T. J. Kang, J. Chen, J. M. Pringle, M. Zhang, A. H. Kazim, S. Fang, C. Haines, D. Al-Masri, B. A. Cola, J. M. Razal, J. Di, S. Beirne, D. R. MacFarlane, A. Gonzalez-Martin, S. Mathew, Y. H. Kim, G. Wallace, R. H. Baughman, *Adv. Mater.* **2017**, *29,* 1605652.